RSC Advances

PAPER

View Article Online
View Journal | View Issue

Cite this: *RSC Adv.*, 2021, **11**, 27965

Assembly of iron oxide nanosheets at the air–water interface by leucine–histidine peptides†

Nina Hoinkis,[a] Helmut Lutz,*[a] Hao Lu,[a] Thaddeus W. Golbek,[b] Mikkel Bregnhøj,[b] Gerhard Jakob,[c] Mischa Bonn[a] and Tobias Weidner*[b]

Received 18th June 2021
Accepted 6th August 2021

DOI: 10.1039/d1ra04733g

rsc.li/rsc-advances

The fabrication of inorganic nanomaterials is important for a wide range of disciplines. While many purely inorganic synthetic routes have enabled a manifold of nanostructures under well-controlled conditions, organisms have the ability to synthesize structures under ambient conditions. For example, magnetotactic bacteria, can synthesize tiny 'compass needles' of magnetite (Fe_3O_4). Here, we demonstrate the bio-inspired synthesis of extended, self-supporting, nanometer-thin sheets of iron oxide at the water–air interface through self-assembly using small histidine-rich peptides.

Since the discovery of magnetotactic bacteria, researchers have been fascinated by the ability of these specialized organisms to orient within the Earth's magnetic field.[1] To be able to react to magnetic fields, magnetotactic bacteria use specialized compartments, called magnetosomes, to produce the iron oxide magnetite (Fe_3O_4). Magnetosomes have a typical size of 30–120 nm and establish a permanent magnetic moment along a fixed axis within the bacteria.[2,3] The magnetization is used to navigate and orient within the terrestrial magnetic field to find favorable living conditions.[4] It has been shown that the size and morphology of magnetic particles used are tightly genetically controlled and vary for different species.[5,6] The biomimetic synthesis of magnetic nanomaterials has been of substantial interest in the past years. Potential applications include biotechnology,[7] medicine[8] and data storage.[9] While the biomimetic preparation of magnetic particles and surface patterns using proteins derived from magnetotactic bacteria has been reported before,[10–12] the biomimetic production of extended 2D magnetic materials using proteins has not been shown. At the same time, 2D nanomaterials have received much attention as ultrathin, high fidelity materials with new properties.[13] Such 2D structures hold great promise as a material that can be self-assembled using effective, low-cost, bottom-up fabrication methods and then tuned chemically to the application.[14] 2D materials can often be synthesized from simple building blocks and are very flexible in terms of surface morphology, porosity, chemical functionality, electronic and magnetic properties. It has been shown that functional 2D inorganic materials can be templated by organic precursor structures at interfaces.[15] In nature, proteins act as the surface "engineers" and steer the growth of minerals at interfaces.[16] 2D materials based on silica, calcium carbonate, and calcium oxalate have been assembled previously by biomimetic peptides at interfaces.[17–19] In this study, we describe the preparation of magnetic 2D materials using peptides mimicking the precipitation of magnetite within magnetosomes.

The processes leading to the production of magnetite is complex and not entirely understood. Faivre *et al.* have suggested the involvement of bi- and trivalent iron ions taken up from sediments and that magnetite is then synthesized *via* templated ferrihydrite precursors.[3] Proton pumps maintain the basic pH required for magnetite formation within the magnetosomes. In analogy to biomineralization of bone, teeth, and shells, the crystal phase and structure of the iron oxide generated have been hypothesized to be controlled by specialized proteins within the magnetosome.[10,12] Sone *et al.* have shown that, within these proteins, histidine sites play an important role because of their ability to chelate Fe^{2+}-ions.[6]

The rationale of this study has been to mimic the precipitation mechanism used by bacteria with a peptide that can precipitate iron oxide 2D sheets and also can effectively bind the air–water interface. We chose a synthetic peptide with the amino acid sequence Ac-LHHLLHLLHHLLHL (short: LHα14, see Fig. 1A), which contains only histidine (H) and leucine (L). In analogy with leucine–lysine (LK) peptides designed by deGrado and Lear,[20] the leucine side chains are intended to bind to the air–water interface, while histidines are expected to be exposed to the water phase and available for interactions with iron ions. The hydrophobic periodicity of 3.5 should favor an α-helical secondary structure at an interface and provide a stable platform for interfacial assembly.[21] The peptide design allows a maximum number of histidines to be exposed to the

[a]*Max Planck Institute for Polymer Research, Ackermannweg 10, 55128 Mainz, Germany. E-mail: helmut.lutz@googlemail.com*

[b]*Department of Chemistry, Aarhus University, Langelandsgade 140, 8000 Aarhus C, Denmark. E-mail: weidner@chem.au.dk*

[c]*University of Mainz, Institute of Physics, Staudinger Weg 7, 55128 Mainz, Germany*

† Electronic supplementary information (ESI) available. See DOI: 10.1039/d1ra04733g

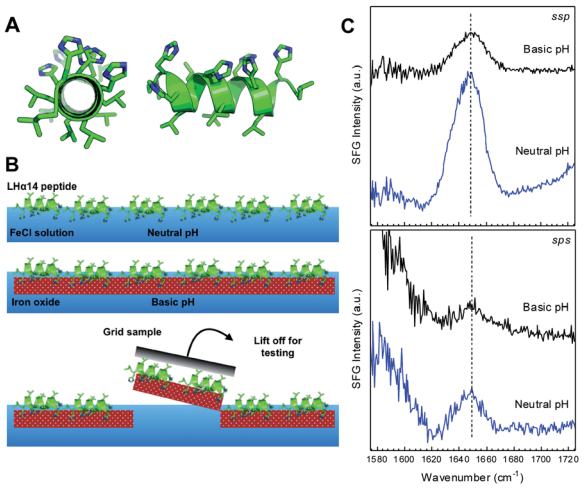

Fig. 1 (A) Front and side view of the LHα14 peptide after energy minimization in bulk water using the software package PEP-FOLD. The sequence is designed to induce a helical fold with hydrophobic leucines for binding to the air–water interface on one side and iron-chelating histidines on the other sides. (B) Schematic of the film formation process. (C) SFG spectra collected with ssp and sps polarization for LHα14 at the solution-air interface before and after the iron precipitation is triggered by increasing the solution pH.

solution phase, while the leucine are intended to stabilize the peptide at the water surface.

We used SFG spectroscopy and surface tension measurements to follow the surface assembly (schematic in Fig. 1B and S1†): first, LHα14 is injected into a Teflon trough with the iron chloride solution at neutral pH. The surface tension increased to 19.1 ± 0.8 mN m^{-1} (measured of 3000 s after stabilization of the film assembly) upon peptide injection, indicating full monolayer coverage of the water surface. The structure of the LHα14 monolayer was determined using sum-frequency generation (SFG) spectroscopy in the amide I region.[22] SFG can probe the secondary structure and orientation of peptides and proteins at liquid surfaces. As second-order nonlinear spectroscopy, SFG is intrinsically surface-specific due to selection rules: SFG is only allowed where inversion symmetry is broken, which is typically the case within an interfacial layer between two bulk isotropic media, such as water and air.[23] Amide I SFG spectra of LHα14 at the FeCl solution surface collected with ssp (s-polarized SFG, s-polarized visible, p-polarized infrared) and sps polarization, are shown in Fig. 1C. Both ssp and sps SFG spectra show a pronounced amide I band centered near 1644 cm^{-1}, which can be assigned to α-helical structure in D_2O.[24]

Following surface adsorption, the subphase was diluted by a factor of eight to reduce the bulk peptide concentration and avoid precipitation in the volume. Subsequently, the pH is increased using ammonia vapor to trigger the precipitation of iron oxide by protonating the histidine sites. SFG spectra recorded in this state (Fig. 1C) show a reduction of the signal level but the resonance position remains unchanged at basic pH. This implies that the secondary structure of LHα14 remains unchanged.

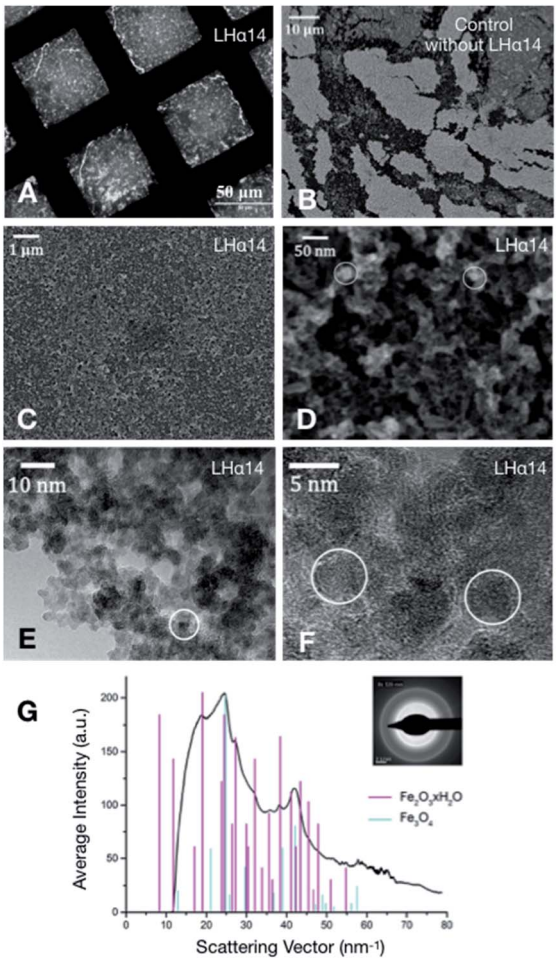

Fig. 2 (A) TEM image of LHα14-templated iron oxide nanosheets spanning the holes of a TEM grid. (B) SEM image of iron oxide film precipitated without peptides and deposited onto a silicon wafer. (C and D) SEM images of LHα14-precipated sheets. (E) TEM image of freestanding nanosheets. The higher resolution TEM in (F) shows crystalline domains. (G) Electron diffraction pattern of the nanosheets.

The interaction of protonated LHα14 with iron ions leads to the precipitation of sheets of iron oxide which can be lifted off the solution surface with transmission electron microscopy (TEM) grids (Fig. 2A). A TEM image of a film transferred from the air–water is shown in Fig. 2A. The sheet covers the openings within the TEM grid and is stable on a length scale of tens of micrometers. Control samples, where iron oxide was precipitated without LHα14, resulted in fragmented and unstable films, as can be seen in the SEM image of a film deposited onto a silicon wafer surface in Fig. 2B. Clearly, the peptides are key to stabilize the iron oxide layer. Higher-resolution SEM images in Fig. 2C and D show the LHα14-precipitated films have a sponge-like porous structure consisting of ~15 nm particles interconnected by wire-like protrusions. Atomic force microscopy (AFM) showed the particles are approximately 20 nm high, leading to the conclusion the particles are roughly spherical (see Fig. 3). The films have a thickness of 22.2 ± 4.3 nm according to AFM line scans across edges of the film.

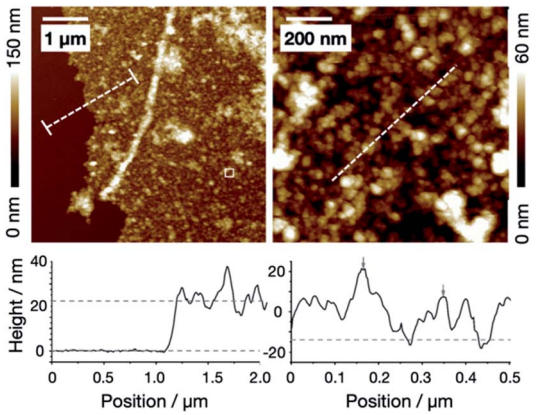

Fig. 3 Atomic force microscopy image of LHα14 precipitated iron oxide nanosheets. (Left) Nanosheet at the edge of a defect to measure the height profile going from the substrate to the iron oxide sheet. The height difference is 22.2 ± 4.3 nm. (Right) Higher magnification image at the position marked in the left panel. The height profile shows an average particle height of 20 nm.

High-resolution TEM images of an edge in the film are displayed in Fig. 2E. It can be clearly seen that the films are free-standing nanosheets and stable without substrate support. The sheets consist of amorphous areas without crystalline structure and crystalline domains of an approximate size of the particles (Fig. 2F). The respective electron diffraction pattern (Fig. 2G) shows the diffraction rings related to the polycrystalline structures. The average intensities as a function of the diffraction angle are plotted along with reference peak positions for ferrihydrite (red) and magnetite (cyan).[25] The ferrihydrite diffraction peaks are generally in good agreement with the experimental peak positions. Some diffraction peaks are not fully resolved within the resolution of the experiment and appear as shoulders (*e.g.* the peak near 27 nm^{-1}). This is likely also the reason the first two ferrihydrite peaks are not visible in the experimental data. Several peak positions and their relative intensities match the typical magnetite diffraction peaks near 24, 37, 39 and 42 nm^{-1}. The data show that the nanosheets contain both magnetite and its precursor ferrihydrite.

X-ray photoelectron spectroscopy (XPS) shows that the sheets contain significant amounts of iron and oxygen as well as the expected nitrogen and carbon from the peptides in the film (Table 1). No contaminations of the sheets have been detected.

The carbon and nitrogen contents of the nanosheets is comparable to that of peptide-based silica and calcium carbonate biomimetic 2D materials.[18,19] Control samples prepared without peptides showed increased amounts of iron and oxygen and negligible nitrogen signals. The carbon signal observed for the control samples is typical for surface preparation under ambient conditions and most likely related to impurity hydrocarbons adsorbed at the air–water interface and the silicon wafer surface (Table 2).

Table 1 Averaged chemical composition of the LHα14 generated sheets along with control films prepared without peptide in atom % standard deviation in parenthesis. The composition is calculated omitting the substrate

	Fe	O	N	C	Si
LHα14	7.6 (0.5)	38.6 (1.0)	2.0 (0.2)	30.4 (0.8)	21.4 (1.2)
Control	10.8 (0.5)	46.4 (2.4)	0.4 (0.1)	27.2 (0.1)	15.1 (1.9)

Table 2 Ratio of Fe and Si XPS intensities and relative film thicknesses for the LHα14-precipitated sheets and the control films

	Fe/Si	Thickness/nm
LHα14	0.4	22.2 (4.3)
Control	0.7	38.8 (6.0)

High-resolution Fe 2p XPS spectra (see Fig. S3 in the ESI†) show peaks near the energy positions expected for the iron oxides Fe_2O_3 and Fe_3O_4 at 724.7 eV and 711.0 eV, related to the Fe $2p_{1/2}$ and Fe $2p_{3/2}$ emission, respectively.[26] In addition, a satellite peak observed near 719 eV is commonly assigned to Fe_2O_3 and the magnetite precursor ferrihydrite. Together, the XPS data show that histidines stabilize iron oxides at the interface.

Conclusions

Histidine-rich LHα14 peptides can precipitate composite iron oxide nanosheets at the air–water interface. The sheets are self-supported, approximately 20 nm thin and at least 50 μm across. The results show that peptide-directed assembly of inorganic materials is a promising approach for the potential fabrication of thin magnetic structures: typical film thicknesses achieved using standard synthesis yield materials with film thicknesses closer to several hundred nanometers.

In future applications, the versatility of peptide amino acid sequences will open up possibilities for tuning the morphology and polymorphism of the nanosheets. The synthesis is, in principle, also compatible with strategies to fabricate 3D structures at the interfaces within emulsions. Generally, the new approach to synthesize nanometer-thin iron oxides may pave the way towards the fabrication of biomimetic magnetic 2D sheets and a low-cost approach to growing magnetic materials with new properties for data storage, sensing and medical applications.

Author contributions

N. H., H. L., H. L., T. W. G., M. B and G. J. performed experiments. All authors analysed data, discussed conclusions and wrote the article.

Conflicts of interest

There are no conflicts to declare.

Acknowledgements

We thank the Villum Foundation (Experiment Grant 22956) and the Novo Nordisk Foundation (Facility Grant NanoScat, No. NNF18OC0032628) for financial support. TWG thanks the Lundbeck Foundation for a postdoc fellowship (R322-2019-2461).

References

1 R. Blakemore, *Science*, 1975, **190**, 377.
2 D. A. Bazylinski and R. B. Frankel, *Nat. Rev. Microbiol.*, 2004, **2**, 217.
3 D. Faivre and D. Schüler, *Chem. Rev.*, 2008, **108**, 4875.
4 (*a*) D. Schüler and R. B. Frankel, *Appl. Microbiol. Biotechnol.*, 1999, **52**, 464; (*b*) K. O. Konhauser, *Earth-Sci. Rev.*, 1998, **43**, 91.
5 (*a*) D. Bertrand, P. Mihály, H. Xin, D. A. Bazylinski, R. B. Frankel and P. R. Buseck, *Am. Mineral.*, 1998, **83**, 1387; (*b*) A. Scheffel, A. Gärdes, K. Grünberg, G. Wanner and D. Schüler, *J. Bacteriol.*, 2008, **190**, 377.
6 E. D. Sone and S. I. Stupp, *Chem. Mater.*, 2011, **23**, 2005.
7 A. K. Gupta and M. Gupta, *Biomaterials*, 2005, **26**, 3995.
8 S. Mornet, S. Vasseur, F. Grasset, P. Veverka, G. Goglio, A. Demourgues, J. Portier, E. Pollert and E. Duguet, *Prog. Solid State Chem.*, 2006, **34**, 237.
9 R. F. Service, *Science*, 2000, **287**, 1902.
10 L. Wang, T. Prozorov, P. E. Palo, X. Liu, D. Vaknin, R. Prozorov, S. Mallapragada and M. Nilsen-Hamilton, *Biomacromolecules*, 2012, **13**, 98.
11 S. M. Bird, A. E. Rawlings, J. M. Galloway and S. S. Staniland, *RSC Adv.*, 2016, **6**, 7356.
12 T. Prozorov, S. K. Mallapragada, B. Narasimhan, L. Wang, P. Palo, M. Nilsen-Hamilton, T. J. Williams, D. A. Bazylinski, R. Prozorov and P. C. Canfield, *Adv. Funct. Mater.*, 2007, **17**, 951.
13 A. Turchanin and A. Gölzhäuser, *Adv. Mater.*, 2016, **28**, 6075.
14 H. Zhao, Y. Zhu, F. Li, R. Hao, S. Wang and L. Guo, *Angew. Chem., Int. Ed.*, 2017, **56**, 8766.
15 (*a*) D. Anselmetti and A. Gölzhäuser, *Angew. Chem., Int. Ed. Engl.*, 2014, **53**, 12300; (*b*) H. Qin, F. Li, D. Wang, H. Lin and J. Jin, *ACS Nano*, 2016, **10**, 948; (*c*) E. J. Robertson, A. Battigelli, C. Proulx, R. V. Mannige, T. K. Haxton, L. Yun, S. Whitelam and R. N. Zuckermann, *Acc. Chem. Res.*, 2016, **49**, 379; (*d*) E. J. Robertson, G. K. Oliver, M. Qian, C. Proulx, R. N. Zuckermann and G. L. Richmond, *Proc. Natl. Acad. Sci. U. S. A.*, 2014, **111**, 13284; (*e*) S. Schrettl, C. Stefaniu, C. Schwieger, G. Pasche, E. Oveisi, Y. Fontana, A. F. i. Morral, J. Reguera, R. Petraglia, C. Corminboeuf, *et al.*, *Nat. Chem.*, 2014, **6**, 468.
16 (*a*) M. Hildebrand, *Chem. Rev.*, 2008, **108**, 4855; (*b*) H. Pyles, S. Zhang, J. J. de Yoreo and D. Baker, *Nature*, 2019, **571**, 251.
17 (*a*) H. Lu, A. Schäfer, H. Lutz, S. J. Roeters, I. Lieberwirth, R. Muñoz-Espí, M. A. Hood, M. Bonn and T. Weidner, *J. Phys. Chem. Lett.*, 2019, **10**, 2170; (*b*) H. Lutz, V. Jaeger, M. Bonn, J. Pfaendtner and T. Weidner, *J. Pept. Sci.*, 2017, **23**, 141.
18 H. Lu, H. Lutz, S. J. Roeters, M. A. Hood, A. Schäfer, R. Muñoz-Espí, R. Berger, M. Bonn and T. Weidner, *J. Am. Chem. Soc.*, 2018, **140**, 2793.
19 H. Lutz, V. Jaeger, L. Schmüser, M. Bonn, J. Pfaendtner and T. Weidner, *Angew. Chem., Int. Ed.*, 2017, **56**, 8277.
20 (*a*) W. F. DeGrado and J. D. Lear, *J. Am. Chem. Soc.*, 1985, **107**, 7684; (*b*) W. F. DeGrado, Z. R. Wasserman and J. D. Lear, *Science*, 1989, **243**, 622.
21 T. Weidner, J. S. Apte, L. J. Gamble and D. G. Castner, *Langmuir*, 2010, **26**, 3433.
22 S. Hosseinpour, S. J. Roeters, M. Bonn, W. Peukert, S. Woutersen and T. Weidner, *Chem. Rev.*, 2020, **120**, 3420–3465.
23 (*a*) Y. R. Shen, *The principles of nonlinear optics*, Wiley-Interscience, New York, 1984; (*b*) A. G. Lambert, P. B. Davies and D. J. Neivandt, *Appl. Spectrosc. Rev.*, 2005, **40**, 103; (*c*) S. Roy, P. A. Covert, W. R. FitzGerald and D. K. Hore, *Chem. Rev.*, 2014, **114**, 8388; (*d*) B. Ding, J. Jasensky, Y. Li and Z. Chen, *Acc. Chem. Res.*, 2016, **49**, 1149.
24 B. R. Singh, in *Infrared analysis of peptides and proteins*, ACS Symposium Series, Washington D. C., 1999.
25 JCPDS International Centre for Diffraction Data, *PDF-2 Database*, Newton Square, USA, 2004.
26 T. Yamashita and P. Hayes, *Appl. Surf. Sci.*, 2008, **254**, 2441.